J Mater Sci (2008) 43:6214–6222
DOI 10.1007/s10853-008-2919-0

Effect of Al content on stacking fault energy in austenitic Fe–Mn–Al–C alloys

Xing Tian · Hong Li · Yansheng Zhang

Received: 2 December 2007 / Accepted: 31 July 2008 / Published online: 26 August 2008

Abstract Effect of Al content on the stacking fault energy (SFE) was investigated in the austenitic Fe–25Mn–(1.16–9.77)Al–0.68C (at%) alloys by X-ray diffraction line profile analysis and thermodynamic estimation, and was discussed on the basis of anomaly in shear modulus caused by the antiferromagnetic transition. The experimental results show that the stacking fault probability decreases with increasing Al content, the observed SFE increases linearly when Al content is lower than 6.27 at%, and markedly as it is more than 6.27 at%. The thermodynamic estimation indicates that the non-magnetic component of SFE increases faster than the observed one with increasing Al content in the antiferromagnetic state, and both are almost equal in the paramagnetic state. The magnetic order increases SFE in the antiferromagnetic state, and the magnetic component of SFE depends on the average magnetic moment and Néel temperature. The increases in the localized magnetic moment and the decrease in the Néel temperature are caused by the addition of Al atoms into the austenitic Fe–Mn alloys and are accompanied by the anomaly in shear modulus, which affects SFE in the antiferromagnetic state. The anomalous drop in shear modulus leads to the inconsistency for the variations of the observed SFE and non-magnetic component with Al content in the antiferromagnetic state.

Introduction

Stacking fault energy (SFE) is one of the most important parameters in materials and is basically affected by composition (electron/atom ratio) and temperature. Many phenomena related to SFE have been widely investigated. For austenitic stainless steels, as an example, the density and distribution of crystal defects, strain-induced transformation, work hardening, and fatigue behavior were explained on the basis of the empirical relationship between SFE and composition. In order to determine SFE, several thermodynamic models and experimental methods were established.

In order to maintain the properties and to decrease the cost of austenitic steels by replacing chromium and nickel entirely or partly, the high-manganese austenitic alloys were widely researched in the past several decades. The effects of alloying elements on the $\gamma \rightarrow \varepsilon$ martensite transformation, β-Mn transition, and mechanical properties in the austenitic Fe–Mn-based alloys have been investigated, and the high-manganese austenitic non-magnetic and cryogenic steels have been successfully developed [1–4]. High-manganese TRIP and TWIP steels, which are used as structural components in automotive vehicle and high power trail of high safety standard, are recently studied [5, 6].

Some studies [1–13] have indicated that aluminum decreases the $\gamma \rightarrow \varepsilon$ transformation temperature, restrains ε-martensite formation, lowers the work hardening, and improves the oxidation and corrosion resistances in austenitic Fe–Mn–Al–C and Fe–Mn–Al–Cr–C alloys. Addition of Al into the austenitic Fe–Mn alloys lowers the Néel temperature and makes the susceptibility–temperature curve exhibits a sharp peak [14, 15]. Previous investigations [16, 17] have pointed out that the antiferromagnetic transition restrains the formation of the thermally induced ε-martensite in the Fe–Mn alloys. According to the stacking fault (SF) mechanism of ε-martensite formation, this effect results from that Al increases SFE in the austenitic Fe–Mn alloys. Hence, it affects also the twinning-induced

X. Tian (✉) · H. Li · Y. Zhang
College of Materials Science and Engineering, Dalian Jiaotong University, Dalian 116028, China
e-mail: xtian_100@yahoo.cn

and $\gamma \rightarrow \varepsilon$ transformation-induced plasticity. Therefore, it is necessary to investigate the effect of Al content and the antiferromagnetic order on SFE in the austenitic Fe–Mn–Al alloys. In this respect, the results of thermodynamic calculations and dislocation node measurement were reported in the literature [8, 18, 19], but the effect of the antiferromagnetic transition was not considered.

The purpose of this work is to investigate the influence of Al content on SFE in the austenitic Fe–25Mn–(1.16–9.77) Al–0.68C (at%) alloys by the X-ray diffraction (XRD) profile analysis and thermodynamic estimation, and to discuss the effect of the antiferromagnetic order. The obtained information is beneficial to elaborate the mechanism of the effect of Al content on the $\gamma \rightarrow \varepsilon$ transformation, deformation mode and work hardening in the austenitic Fe–Mn–Al alloys.

Method for determination

XRD line profile analysis

For the experimental determination of SFE, both direct and indirect methods are usually used. The direct one is often the observation of extended dislocation nodes by TEM and is considered to be especially accurate for the materials with the low SFE [20, 21]. The indirect one is the combined measurement of SF probability and rms microstrain by XRD line profile analysis (XRDLPA) [22–24]. Mukherjee et al. [25] compared the two methods and pointed out that only a miniscale volume of the material ($\sim$100 μm^3) is examined under TEM in a thin foil at a time, thus, it cannot depict the microstructure of the bulk materials. In addition, some changes may be produced in the defect structure during preparation of the thin foils, and the strain fields related to the dislocations present in the microstructure may relax in sectioning and polishing. Therefore, the reliability for measurement of microstructure parameters depends on whether the thin area is a representative of microstructure of the entire specimen. XRDLPA evaluates the microstructure parameters in a statistical manner, averaged over a volume of 10^9 μm^3. This analysis is much easier, more reliable, and quicker and has become a powerful technique with improving the software for the microstructure characterization by the profile fitting. Thus, this technique is still used to determine SFE [26, 27].

The residual stresses, intrinsic SF, and change in lattice parameter lead to the peak shift of diffraction line profile. The broadening results from the reduction in the size of coherently diffracting domains, faults on certain planes and strains produced by dislocations in these domains. However, the broadening caused by the intrinsic SFs is symmetrical, while one due to the twin and extrinsic SFs is asymmetrical. For cold work powder, the effect of residual stress is very small and can be neglected. If the peak position is measured near the top of peak, and the effect due to the change in lattice parameter also is small, then the peak shift may be only regard as stemming from the intrinsic SFs. In order to avoid diffractometer zero error, the relative shifts of neighboring $(h_1k_1l_1)$ and $(h_2k_2l_2)$ reflections from the filed and annealed powders, $\Delta 2\theta$, can be obtained. The SF probability, α, may be determined from following equation [24]

$$\begin{aligned}\Delta 2\theta &= (2\theta_{200} - 2\theta_{111})_{\mathrm{CW}} - (2\theta_{200} - 2\theta_{111})_{\mathrm{ANN}} \\ &= -\frac{45\sqrt{3}}{\pi^2}\left(\tan\theta_{200} + \frac{1}{2}\tan\theta_{111}\right)\alpha, \end{aligned} \quad (1)$$

where 2θs are the line position in degree; $(2\theta_{200} - 2\theta_{111})_{\mathrm{CW}}$ and $(2\theta_{200} - 2\theta_{111})_{\mathrm{ANN}}$ the difference between (200) and (111) peak positions for the cold-worked powder and annealed (standard) specimens.

After correction for the instrumental broadening, the broadened line profile can be expressed as a Fourier series. According to the Warren and Averbach method of Fourier analysis of line profile [28], the values of order-dependent rms microstrain, $\langle \varepsilon_L^2 \rangle_{hkl}$, may be obtained

$$\langle \varepsilon_L^2 \rangle_{hkl} = \frac{[\ln A_L(h_1k_1l_1) - \ln A_L(h_2k_2l_2)]a_0^2}{2\pi^2 L^2[(h_2^2 + k_2^2 + l_2^2) - (h_1^2 + k_1^2 + l_1^2)]}, \quad (2)$$

where $A_L(h_1k_1l_1)$ and $A_L(h_2k_2l_2)$ are the coefficients of cosine term with the first power in the Fourier series, $(h_1k_1l_1)$ and $(h_2k_2l_2)$ the indices of diffraction planes, L a length normal to the reflecting planes, and a_0 is the lattice parameter of the standard.

For the reflections of (111), (200), and (222), α and the rms microstrain in $\langle 111 \rangle$ direction averaged over the length of 5 nm, $\langle \varepsilon_{50}^2 \rangle_{111}$, can be obtained from Eqs. 1 and 2. Further, SFE can be calculated according to the following equation [24]

$$\gamma = \frac{K_{111}\omega_0 G_{(111)} a_0 A^{-0.37}}{\pi\sqrt{3}} \frac{\langle \varepsilon_{50}^2 \rangle_{111}}{\alpha}, \quad (3)$$

where $K_{111}\omega_0 = 6.6$ is proportionality constant, $G_{(111)}$ $(=[C_{44} + C_{11} - C_{12}]/3)$ the shear modulus in the (111) plane, $A(=2C_{44}/[C_{11} - C_{12}])$ Zener anisotropy coefficient, C_{11}, C_{12}, and C_{44} are elastic stiffness coefficients. If the parameters $G_{(111)}$, A, a_0, $\langle \varepsilon_{50}^2 \rangle_{111}$, and α were experimentally measured, SFE can be determined.

Thermodynamic estimation

SF in fcc (γ) crystal can be regarded as two layers of hcp (ε) phase. On the basis of the Hirth's review on the thermodynamics of SF [29], SFE is expressed as [30–32]

$$\gamma = 2\rho\Delta G^{\gamma\to\varepsilon} + 2\sigma^{\gamma/\varepsilon}, \tag{4}$$

where ρ is the molar surface density in a close packed plane, $\Delta G^{\gamma\to\varepsilon}$ the molar free energy difference between the γ- and ε-phases, and $\sigma^{\gamma/\varepsilon}$ the interface energy of the $\gamma - \varepsilon$ phases. The value of $\sigma^{\gamma/\varepsilon}$ is generally taken between 5 and 15 mJ/m^2 for transition metals [33]. The molar surface density is given as

$$\rho = \frac{4}{\sqrt{3}Na_0^2}, \tag{5}$$

where a_0 is lattice parameter and N is Avogadro's number.

On the basis of the regular solution model, the molar-free energy difference between the γ- and ε-phases, $\Delta G^{\gamma\to\varepsilon}$, can be calculated from the following equation

$$\Delta G^{\gamma\to\varepsilon} = \sum_i^n X_i \Delta G_i^{\gamma\to\varepsilon} + \frac{1}{2}\sum_i^n \sum_j^n X_i X_j \Delta\Omega_{ij}^{\gamma\to\varepsilon} + \Delta G_{\mathrm{m}}^{\gamma\to\varepsilon} + \Delta G_{\mathrm{seg}}, \tag{6}$$

where X_i and X_j are the molar fractions of pure component i and j; $\Delta G_i^{\gamma\to\varepsilon}$ is the molar-free energy difference between the γ- and ε-phases for pure component i, $\Delta\Omega_{ij}^{\gamma\to\varepsilon}$ the interaction parameter difference for pure components i and j in the γ- and ε-phases, $\Delta G_{\mathrm{m}}^{\gamma\to\varepsilon}$ the molar magnetic-free energy difference between the γ- and ε-phases, and ΔG_{seg} the free energy change due to the Suzuki effect and is not usually considered at low temperature [34]. The sum of first two terms in Eq. 6 is the non-magnetic component of $\Delta G^{\gamma\to\varepsilon}$.

In the spontaneous magnetization, the order–disorder transition of magnetic moment and spontaneous volume magnetostriction will occur, and the magnetic elastic stress appears, which have contribution to the magnetic-free energy. Since the macroscopic intensity of magnetization is zero in the spontaneous magnetic transition, the magnetic-free energy at the constant pressure, G_{m}, can be given as

$$G_{\mathrm{m}} = -T\,\mathrm{d}S + p\Delta V, \tag{7}$$

where $-T\,\mathrm{d}S = G_{\mathrm{ms}}$ is the free energy produced by the change in the magnetic entropy and $p\Delta V$ is the work done by the spontaneous volume expansion. The investigation of the austenitic Fe–Mn–Si–C alloys has shown that $p\Delta V$ may be ignored in comparison with the non-magnetic component of $\Delta G^{\gamma\to\varepsilon}$, which will be described elsewhere.

According to Hirllert and Jar [35], the magnetic-free energy caused by the entropy change in ϕ-phase is expressed as

$$G_{\mathrm{m}}^{\varphi} = RT\ln(\beta^{\varphi}+1)f^{\varphi}(\tau^{\varphi}), \tag{8}$$

where β^{φ} is the average atomic magnetic moment (in Bohr magnetons), T_{C}^{φ} the critical temperature of magnetic transition, $\tau^{\varphi} = T/T_{\mathrm{C}}^{\varphi}$ the scaled temperature, and $f^{\varphi}(\tau^{\varphi})$ a polynomial function of τ^{φ}.

Experimental

The tested alloys used in this work were melted in an induction furnace at atmospheric pressure from commercially pure iron, aluminum, and metallic manganese. The ingots about 25 kg in weight were held at 1,423 K for 1.5 h, and forged into 20 × 20 mm^2 bars. Their major chemical composition, lattice parameter, a_0, Néel temperature, T_{N}^{γ}, and mean electron concentration, e/a, are listed in Table 1 [14, 36].

Shear modulus for the tested alloys was measured by the audio resonance method at room temperature and is also listed in Table 1. The Young's modulus–temperature curve was founded with the dynamic method by measuring the resonance frequency of transverse vibrations excited in a horizontally suspended specimen with the diameter of 6 mm and length of 160 mm and heated at the rate of 0.5 K/min.

In order to reduce the influence of preferred orientation caused by coarse grains, cold-worked powder was prepared by filing the uniformly strained portions of the tensile sample, which was strained to fracture and solution treated at 1,273 K for 0.5 h. The preparation was carried out at room temperature, and the over rise of the sample temperature must be avoided as far as possible. The cold-worked powder was sifted through a screen of 250 meshes, and the fine powder (≤40 μm) was used for XRD. Standard specimen was prepared from portion of the fine powder. This portion of the fine powder was wrapped in nickel foil and was sealed in fused silica tube filled with pure argon at the pressure of 6.7 × 10^4 Pa, and homogenized at 1,273 K for 3 h.

XRD was carried out on a D/MAX-RA X-ray diffractometer with a rotating target using monochromated CuKα radiation at room temperature. A step-scanning rate of 0.02° was selected. The (111), (200), and (222) line profiles of the powder and standard specimens were recorded at time interval of 1 s with a 0.3 mm detector slit. Three powder specimens were examined at least for each tested alloy. After the recorded diffraction line profile was smoothed down to seven points and was corrected for

Table 1 Major chemical compositions (at%), lattice parameter, a_0, Néel temperature, T_{N}^{γ}, shear modulus, G, and mean electron/atom ratio, e/a, for the tested alloys

Alloy	Al	Mn	C	Fe	a_0 (nm)	T_{N}^{γ} (K)	G (GPa)	e/a
FA1	1.16	25.59	0.69	72.25	0.36101	380	6.472	7.61
FA2	3.16	24.75	0.69	71.18	0.36162	372	6.532	7.52
FA3	4.45	24.47	0.67	70.31	0.36175	368	6.535	7.47
FA4	6.27	24.80	0.68	68.10	0.36246	353	6.586	7.37
FA5	9.77	23.78	0.66	65.64	0.36339	284	6.964	7.21

background intensity and Lorentz-polarization factor, the $K\alpha_1$ and $K\alpha_2$ components were separated according to the imitative functions, and the peak positions were determined. Using the specified software, the physical profile was obtained from the $K\alpha_1$ component.

Results and discussion

SFE determination

For each powder specimen, the relative peak shift, $\Delta 2\theta$, can be obtained from the peak positions of (111) and (200) reflections for the powder and standard specimens, and α can be calculated according to Eq. 1. The averaged value for each tested alloy is listed in Table 2. α decreases linearly with increasing Al content, as shown in Fig. 1, and is given as

$$\alpha \times 10^{-3} = 38.41 - 3.259(\text{Al at\%}). \quad (9)$$

The physical profiles of (111) and (222) reflections were transferred into the Fourier series by the fast Fourier transformation program, and the coefficients of cosine term with the first power in the Fourier series, $A_L(111)$ and $A_L(222)$, were obtained. Using $A_L(111)$, $A_L(222)$ and the lattice parameter listed in Table 1, the rms microstrain for each powder specimen, $\langle \varepsilon_{50}^2 \rangle_{111}$, can be calculated by Eq. 2. The averaged value for each tested alloy is also listed in Table 2.

The parameters $G_{(111)}$ and A in Eq. 3 are usually measured on single crystal. For the austenitic Fe–Mn–Al–C alloys, the elastic stiffness coefficients, C_{11}, C_{12}, and C_{44}, have not been reported in literature until now. However, using $A = 3.43$ for the austenitic stainless steels [24], $\gamma/G_{(111)}$ can be calculated from Eq. 3 and may be used to express the effect of Al content on SFE in the tested alloys. The averaged value of $\gamma/G_{(111)}$ for each tested alloy is listed in Table 2 and varies with Al content.

If the tested alloys are considered to be isotropic, and $G_{(111)}$ may be replaced with the macroscopic shear modulus G, then SFE can be calculated and is named as the observed SFE, γ_{ob}. The averaged value of γ_{ob} for each tested alloy is also listed in Table 2, and the variation of γ_{ob} with Al content is shown in Fig. 2, i.e., γ_{ob} increases linearly when Al content is lower than 6.27 at% and more markedly as it is more than 6.27 at%.

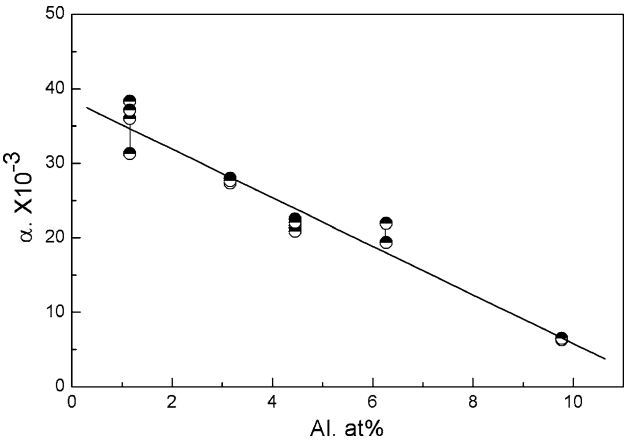

Fig. 1 Variation of SF possibility α with Al content

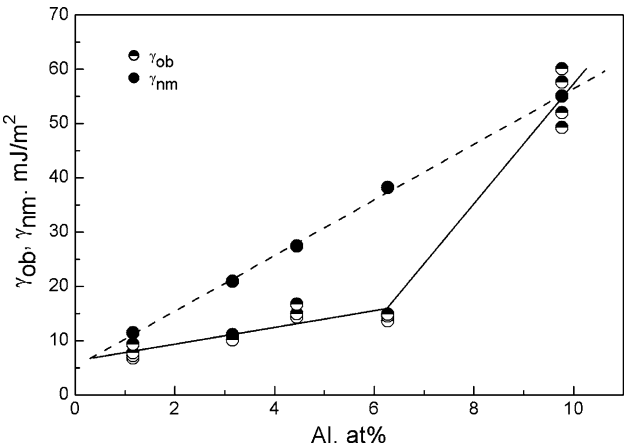

Fig. 2 Variations of the observed SFE and non-magnetic component, γ_{ob} and γ_{nm}, with Al content

Scatter for the SF probability, rms microstrain and $\gamma/G_{(111)}$ value are higher, as shown in Table 2. The reason for the appearance of the scatter includes: (1) the strain-

Table 2 XRD parameters for the tested alloys

Alloy	Al (at%)	Δ ($\Delta 2\theta$°)	$\alpha \times 10^{-3}$	$\langle \varepsilon_{50}^2 \rangle_{111} \times 10^{-6}$	$\gamma/G_{(111)} \times 10^{-13}$	γ_{ob} (mJ/m^2)
FA1	1.16	0.191 (0.018)	36.04 (3.35)	15.45 (1.52)	1.20 (0.24)	7.75 (1.57)
FA2	3.16	0.146 (0.002)	27.65 (0.31)	16.24 (0.84)	1.63 (0.08)	10.67 (0.55)
FA3	4.45	0.114 (0.004)	21.66 (0.81)	18.01 (1.22)	2.31 (0.03)	15.12 (1.58)
FA4	6.27	0.113 (0.011)	21.37 (2.03)	16.85 (0.69)	2.21 (0.32)	14.95 (1.69)
FA5	9.77	0.033 (0.001)	6.35 (0.11)	17.86 (1.84)	7.86 (0.78)	54.74 (5.34)

Data in brackets express the maximum deviation

induced $\gamma \rightarrow \varepsilon$ transformation caused in filing powder of alloy FA1 relaxes the strain state in austenite because the ε-phase volume is smaller than the γ-phase; (2) the larger grain size (30–40 μm) can cause the inhomogeneous strain in the filed powder; (3) temperature of cold-worked powder can rise during filing, the positive magnetostriction caused by the antiferromagnetic transition appears on cooling and overlaps over microstrain due to filing. Therefore, the relative error is about 20% for alloy FA1, and is lower than 11.3% for the others.

Thermodynamic estimation

In the tested alloys, the γ and ε-phases undergo the antiferromagnetic transition and have the respective Néel temperature. For the estimation of SFE, in addition to the lattice parameter and Néel temperature, the correlative phase stability and magnetic parameters must be know for the γ- and ε-phases.

Non-magnetic component

Let us select first the parameters in the non-magnetic component, i.e., the first two terms in Eq. 6. The values of parameters $\Delta G_{\mathrm{Fe}}^{\gamma\rightarrow\varepsilon}$, $\Delta G_{\mathrm{Mn}}^{\gamma\rightarrow\varepsilon}$, and $\Delta G_{\mathrm{C}}^{\gamma\rightarrow\varepsilon}$ at 300 K are taken from Refs. [37–39], i.e., $\Delta G_{\mathrm{Fe}}^{\gamma\rightarrow\varepsilon} = -266.8$, $\Delta G_{\mathrm{Mn}}^{\gamma\rightarrow\varepsilon} = 3,458.6$, and $\Delta G_{\mathrm{C}}^{\gamma\rightarrow\varepsilon} = -2,467\,\mathrm{J/mol}$. $\Delta G_{\mathrm{Al}}^{\gamma\rightarrow\varepsilon}$ can be estimated from the temperature dependence of SFE in pure aluminum and molar volume (10 cm^3/mol) [40]. According to Ericsson's analysis [41], SFE in pure metal may be considered to be almost the same as the free energy difference between γ- and ε-phases with one atomic layer

$$\gamma = \frac{\Delta G^{\gamma\rightarrow\varepsilon}}{N_0^{1/3}V^{2/3}}, \tag{10}$$

where N_0 is Avogadro's number, and V the molar volume of pure metals. $\Delta G_{\mathrm{Al}}^{\gamma\rightarrow\varepsilon}$ is derived from this equation to be 6,502 J/mol at 300 K.

Lee and Choi [32] examined $\Delta\Omega_{\mathrm{FeMn}}^{\gamma\rightarrow\varepsilon} = -10,837 + 22,887X_{\mathrm{Mn}}$ J/mol given by Ishida and Nishizawa [42] and found that the calculated $T_0^{\gamma\rightarrow\varepsilon}$(=[$M_{\mathrm{S}} + A_{\mathrm{S}}$]/2) is higher in the Fe–(13–28)Mn alloys. $\Delta G_{\mathrm{FeMn}}^{\gamma\rightarrow\varepsilon}$ has been corrected to be $-9,135.5 + 15,282.1X_{\mathrm{Mn}}$. The parameters $\Delta G_{\mathrm{FeAl}}^{\gamma\rightarrow\varepsilon}$ and $\Delta G_{\mathrm{FeC}}^{\gamma\rightarrow\varepsilon}$ are estimated from the appropriate equations [42]

$$\Delta G_X^{\gamma/\varepsilon\mathrm{Fe}} \approx \Delta G_{\mathrm{Fe}}^{\gamma\rightarrow\varepsilon} - \frac{\mathrm{d}\Delta G_{\mathrm{Fe}}^{\gamma\rightarrow\varepsilon}}{\mathrm{d}T}\frac{(1 - X_{\mathrm{Mn}} - X_X)\Delta T_0^{\gamma\rightarrow\varepsilon}}{X_X}, \tag{11}$$

$$\Delta G_X^{\gamma/\varepsilon\mathrm{Fe}} = \Delta G_X^{\gamma\rightarrow\varepsilon} + \Delta\Omega_{\mathrm{Fe}X}^{\gamma\rightarrow\varepsilon}, \tag{12}$$

where $\Delta G_X^{\gamma/\varepsilon\mathrm{Fe}}$ is the effect of component X on the relative stability between γ-Fe and ε-Fe, and $\Delta T_0^{\gamma\rightarrow\varepsilon}$ the change in $T_0^{\gamma\rightarrow\varepsilon}$ temperature of the Fe–Mn alloys produced by component X. $\frac{\mathrm{d}}{\mathrm{d}T}(\Delta G_{\mathrm{Fe}}^{\gamma\rightarrow\varepsilon})$ is estimated from $\Delta G_{\mathrm{Fe}}^{\gamma\rightarrow\varepsilon}$ in Ref. [37] to be about 3.264 J mol^{-1} K^{-1} at 300 K. Using the change in the $T_0^{\gamma\rightarrow\varepsilon}$ of the Fe–Mn alloys caused by Al and C (28 and 48 K/at%) [42], $\Delta G_{\mathrm{Al}}^{\gamma/\varepsilon\mathrm{Fe}}$ and $\Delta G_{\mathrm{C}}^{\gamma/\varepsilon\mathrm{Fe}}$ derived from Eq. 11 are −9,109 and −15,639 J/mol in the Fe–25(at%)Mn at 300 K, then $\Delta\Omega_{\mathrm{FeAl}}^{\gamma\rightarrow\varepsilon} = 2,598$ and $\Delta G_{\mathrm{FeC}}^{\gamma\rightarrow\varepsilon} = 3,990\,\mathrm{J/mol}$. The contributions of $\Delta\Omega_{\mathrm{MnC}}^{\gamma\rightarrow\varepsilon}$, $\Delta\Omega_{\mathrm{MnAl}}^{\gamma\rightarrow\varepsilon}$ and $\Delta\Omega_{\mathrm{AlC}}^{\gamma\rightarrow\varepsilon}$ and the interactions along three components, such as $\Delta\Omega_{\mathrm{FeMnC}}^{\gamma\rightarrow\varepsilon}$ and $\Delta\Omega_{\mathrm{MnAlC}}^{\gamma\rightarrow\varepsilon}$, are so small that it can be neglected [8]. The non-magnetic component of $\Delta G^{\gamma\rightarrow\varepsilon}$, $\Delta G_{\mathrm{nm}}^{\gamma\rightarrow\varepsilon}$, can be calculated from the above parameters. The calculated non-magnetic component of SFE, γ_{nm}, is shown in Fig. 2 and is given as

$$\gamma_{\mathrm{nm}}(\mathrm{mJ/m^2}) = 5.18 + 5.124(\mathrm{Al\ at\%}). \tag{13}$$

Magnetic component

Since the γ- and ε-phases undergo the antiferromagnetic transition, $\Delta G_{\mathrm{m}}^{\gamma\rightarrow\varepsilon}$ is

$$\Delta G_{\mathrm{m}}^{\gamma\rightarrow\varepsilon} = G_{\mathrm{m}}^{\varepsilon} - G_{\mathrm{m}}^{\gamma}, \tag{14}$$

where G_{m}^{γ}, $G_{\mathrm{m}}^{\varepsilon}$ is the magnetic-free energy of the γ- and ε-phases, respectively. Since $p\Delta V$ is so small that it may be ignored in comparison with $\Delta G_{\mathrm{nm}}^{\gamma\rightarrow\varepsilon}$, G_{m}^{γ} and $G_{\mathrm{m}}^{\varepsilon}$ can be approximately expressed by Eq. 8. According to Hirllert and Jar [35], $f^{\varphi}(\tau^{\varphi})$in Eq. 8 is given as

$$f^{\varphi}(\tau^{\varphi}) = 1 - \frac{1}{D}\left\{\frac{79\tau^{-1}}{140p} + \frac{474}{497}\left[\frac{1}{p} - 1\right]\left[\frac{\tau^3}{6} + \frac{\tau^9}{135} + \frac{\tau^{15}}{600}\right]\right\} \quad (\tau = T/T_{\mathrm{C}}^{\varphi} > 1), \tag{15}$$

$$f^{\varphi}(\tau^{\varphi}) = -\frac{1}{D}\left[\frac{\tau^{-5}}{10} + \frac{\tau^{-15}}{315} + \frac{\tau^{-25}}{1500}\right] \quad (\tau = T/T_{\mathrm{C}}^{\varphi} > 1), \tag{16}$$

$$D = \frac{518}{1125} + \frac{11692}{15975}\left(\frac{1}{p} - 1\right),$$

where p is only dependent on crystal structure. For fcc and hcp crystals, p = 0.28 [43]. In the present case, ϕ represents the γ- and ε-phases, and T_{C}^{φ} the Néel temperature of both phases, T_{N}^{γ} and $T_{\mathrm{N}}^{\varepsilon}$. $\Delta G_{\mathrm{m}}^{\gamma\rightarrow\varepsilon}$ in Eq. 6 implies the change in the magnetic-free energy caused by the antiferromagnetic transition. In order to determine $\Delta G_{\mathrm{m}}^{\gamma\rightarrow\varepsilon}$, T_{N}^{γ} and $T_{\mathrm{N}}^{\varepsilon}$, $\beta^{\gamma}$and β^{ε} must be known.

Concerning $G_{\mathrm{m}}^{\varepsilon}$, Ishida [34] and Petrov and Yakubtsov [44] considered that the ε-phase is non-magnetic in most metals and $G_{\mathrm{m}}^{\varepsilon} = 0$. However, the ε-phase undergoes the antiferromagnetic transition in the Fe–Mn alloys. Ohno and Mekata [45] showed that the antiferromagnetic transition occurs at 230 K for the ε-phase in the Fe–(17.8–28.6)Mn alloys, and the magnetic moment β^{ε} is $\sim$0.25 μ_{B}. They

Table 3 Magnetic-free energy $\Delta G_m^{\gamma\to\varepsilon}$ and magnetic component of SFE for the tested alloys

Alloy	Al (at%)	T/T_N^γ	$f^\gamma(\tau^\gamma)$	$\Delta G_m^{\gamma\to\varepsilon} = -G_m^\gamma$ J/mol	$\gamma_m \times 10^{-2}$ (mJ/m^2)
FA1	1.16	0.789	−0.17660	440.487 $\ln(\beta^\gamma + 1)$	2.592 $\ln(\beta^\gamma + 1)$
FA2	3.16	0.806	−0.15953	397.911 $\ln(\beta^\gamma + 1)$	2.334 $\ln(\beta^\gamma + 1)$
FA3	4.45	0.815	−0.15120	377.138 $\ln(\beta^\gamma + 1)$	2.211 $\ln(\beta^\gamma + 1)$
FA4	6.27	0.850	−0.12138	302.769 $\ln(\beta^\gamma + 1)$	1.768 $\ln(\beta^\gamma + 1)$
FA5	9.77	1.056	−0.03313	82.625 $\ln(\beta^\gamma + 1)$	0.499 $\ln(\beta^\gamma + 1)$

considered that the Néel temperature of the ε-phase is composition-independent in the Fe–(17.8–28.6)Mn alloys. T_N^ε and β^ε will be affected by the Al content in the Fe–Mn–Al alloys, and the relative results have been not reported in literature. Considering that the magnetic order cannot disappear completely above T_N^ε, the free energy caused by the change in the magnetic entropy, G_{ms}^ε, should be estimated. G_m^ε calculated from $T_N^\varepsilon = 230$ K and $\beta^\varepsilon = 0.25\,\mu_B$ is only −6.306 J/mol at 300 K and can be ignored in comparison with $\Delta G_{nm}^{\gamma\to\varepsilon}$, that it, $\Delta G_m^{\gamma\to\varepsilon} = -G_m^\gamma$.

The Néel temperature decreases with increasing Al content in the tested alloys, and $f^\gamma(\tau^\gamma)$ calculated from Eqs. 15 and 16 are smaller than zero and increase with increasing Al content, as shown in Table 3. The average magnetic moment is usually measured by means of Neutron diffraction, but the quantitative effect of Al content on β^γ in the austenitic Fe–Mn–Al alloys is not available in literature. Al and Si belong to non-transition elements and are possessed of the analogous electronic structure of outer shell ($3s^23p^1$ and $3s^23p^2$), and the austenitic Fe–Mn–Al–C and Fe–Mn–Si–C alloys exhibit the analogous susceptibility–temperature curves [15, 46]. The Mössbauer spectra study on the austenitic Fe–Mn–Si–C alloys shows that the addition of Si increases the localized magnetic moment on Fe atom sites and the hyperfine field below T_N^γ [47]. It is expected from these that the localized magnetic moment at Fe atom sites increases with increasing Al content. The decrease in mean electron concentration (e/a) with increasing Al content also indicates that the addition of Al into the austenitic Fe–Mn alloys increases the atomic magnetic moment. Although the relationship between β^γ and Al content is not available, the dependence of $\Delta G_m^{\gamma\to\varepsilon}$ on β^γ has been obtained at 300 K and is listed in Table 3. Since $\ln(\beta^\gamma + 1)$ and $-f^\gamma(\tau^\gamma)$ are larger than zero, $\Delta G_m^{\gamma\to\varepsilon}$ is positive. Therefore, the magnetic component of SFE depends on the product of $\ln(\beta^\gamma + 1)$ and $-f^\gamma(\tau^\gamma)$ at the given temperature and increases SFE in the antiferromagnetic state. The relationship between γ_m and β^γ has been obtained at 300 K and is listed in Table 3. For alloy FA5, since it is in paramagnetic state at 300 K, the magnetic component of SFE, γ_m, is $4.99 \times 10^{-3} \ln(\beta^\gamma + 1)$ mJ/m^2 and may be neglected, and γ_{ob} is approximately equal to γ_{nm}. If the quantitative dependence of β^γ on Al content could be obtained, the influence of Al on the magnetic component will be quantitatively established in the tested alloys.

Discussion

It is seen from Fig. 2 that, in the range of Al content lower than 6.27 at%, the observed SFE is lower and increases with increasing Al content slower than the non-magnetic component because alloys FA1–FA4 are in the antiferromagnetic state at 300 K. If the magnetic component is added in, the difference between the observed and the thermodynamically estimated SFEs will increase. However, the observed SFE and non-magnetic component are almost equal in alloy FA5 that is in the paramagnetic state at 300 K. These facts show that the antiferromagnetic transition affects markedly SFE in the tested alloys.

Effect of shear modulus on SFE

Equation 3 shows that the observed SFE depends on the parameters a_0, G, $\langle\varepsilon_{50}^2\rangle_{111}$ and α since $K_{111}\omega_0$ and A were selected as constants, and $G_{(111)}$ is replaced by the macroscopic shear modulus G in the present work.

For the tested alloys, the shear modulus is affected by the Al content and antiferromagnetic transition. The elastic modulus–temperature curve for the tested alloys is shown in Fig. 3. The elastic modulus decreases with increasing Al content in the paramagnetic state, however, the anomalous drop in the elastic modulus, called as the "ΔE" effect, appears below the Néel temperature. The "ΔE" effect originates from the lattice expansion and the decrease in atom band energy caused by the antiferromagnetic transition and reduces with increasing Al content in the tested alloys. It may be expected that the shear modulus G and $G_{(111)}$ also exhibit the same character. The macroscopic shear modulus for the tested alloys, G, increases with increasing Al content at room temperature, as shown in Fig. 4. Because alloy FA5 is in the paramagnetic state at 300 K, its macroscopic shear modulus is markedly higher than that for the other alloys. Although the changes in a_0 and $\langle\varepsilon_{50}^2\rangle_{111}$ are small, the variation of shear modulus with

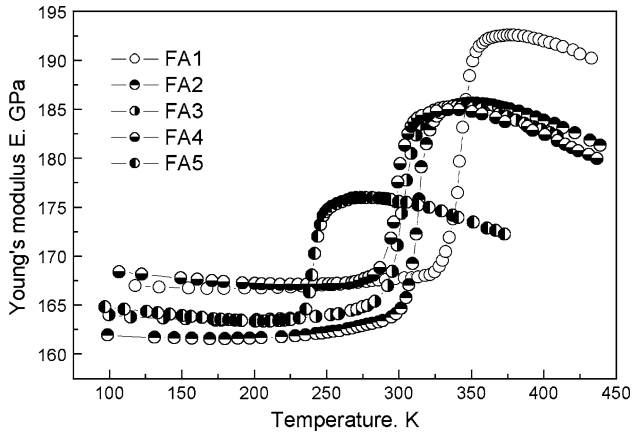

Fig. 3 Young's modulus–temperature curves for the tested alloys

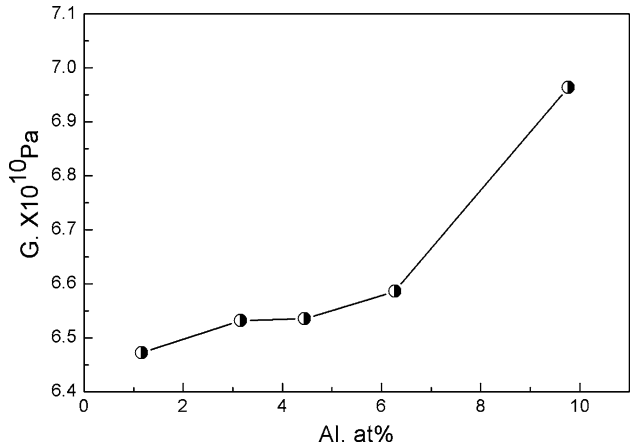

Fig. 4 Shear modulus of the tested alloys at room temperature

Al content makes α decrease linearly. Therefore, the anomaly of shear modulus caused by the antiferromagnetic transition is the reason why the observed SFE is lower than the non-magnetic component and increases slowly with increasing Al content in the range of Al content lower than 6.27 at%, however, this effect is not considered in the thermodynamic estimation. For alloy FA5, the observed SFE is close to the non-magnetic component of SFE because it is in the paramagnetic state at 300 K and there is not the effect of the anomalous drop in the shear modulus.

In order to verify the variation of the observed SFE with Al content in the tested alloys, the tensile specimens were prepared from the bars treated at 1,273 K for 1 h and air-cooled and then were strained to fracture at room temperature. The deformation structure in the uniformly strained portions of fractured tensile specimens was examined by XRD. The result indicates that the strain-induced ε-martensite appears only in alloy FA1, as shown in Fig. 5, and was not detected in the others. The deformation structure in the tested alloys has been also observed by TEM [13]. The

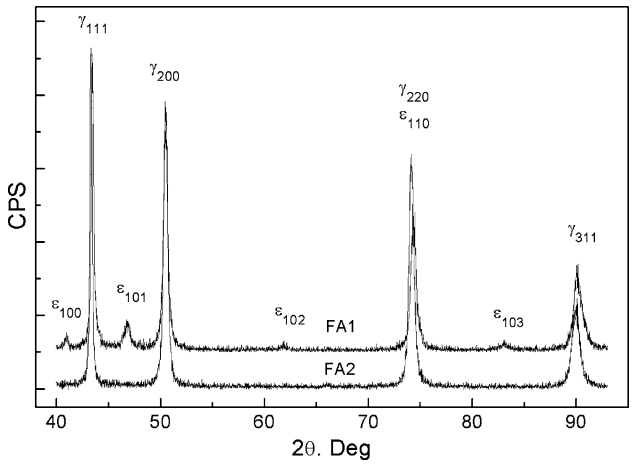

Fig. 5 XRD patterns of the uniform portions for Alloy FA1 and FA2 after tensile test at room temperature

deformation structure shifts from the strain-induced ε-martensite and strain-induced twins to the strain-induced twins and dislocation cell structure with increasing Al content, and the size of dislocation cell structure reduces correspondingly. The strain-induced ε-martensite was detected also in alloy FA2 under TEM. Thus, the strain-induced $\gamma \rightarrow \varepsilon$ transformation occurs at SFE lower than 12 mJ/m^2, and the strain-induced twinning at SFE higher than 10 mJ/m^2. These results conform to the dependence of deformation structure on SFE [48] and also verify that the addition of Al increases SFE in the tested alloys.

Effect of Al content on the magnetic component of SFE

Now let us discuss the effect of Al content on the magnetic component of SFE. The increase in the non-magnetic component of SFE with increasing Al content is due to the increases in the configurational entropy caused by the addition of Al into the austenitic Fe–Mn alloys. However, the effect of Al content on SFE is also shown by its influence on the shear modulus, average magnetic moment per atom, and Néel temperature for the tested alloys. This has been testified by the fact that the observed SFE is lower than the non-magnetic component of SFE in the antiferromagnetic state since it reflects the synthesized effect of Al content. Therefore, the effect of Al content on the antiferromagnetic transition is the main reason why the inconsistency for the variation of the observed SFE and non-magnetic component with Al content in the antiferromagnetic state.

In the austenitic Fe–Mn alloys, the magnetic susceptibility does not obey the Curie–Weiss law above T_N^{γ} and is independent of temperature, the hyperfine field is not affected by the surroundings, and there is no localized magnetic moment on the Fe atom site [49]. In the austenitic

Fe–Mn–Al–C alloys, the magnetic susceptibility exhibits the stronger temperature and composition dependence [14, 15]. Although the Mössbauer spectra study on the austenitic Fe–Mn–Al alloys is not reported in the literature yet, it may be expected from the comparison with the austenitic Fe–Mn–Si–C alloys that the hyperfine field is affected by surroundings, and there is the localized magnetic moment [47, 48]. Since Al is a non-transition element with $3s^2 3p^1$ outer electron configuration, only the localized magnetic moment develops on the Fe atom sites, that is, the addition of Al atoms into the austenitic Fe–Mn alloys induces the localized magnetic moment on the Fe atom sites. Qin and Zhang [47] attributed this phenomenon to that the valence electronic band of Al overlaps over the d band of the matrix. The energy required by the order–disorder transition of magnetic moment is offered by decreasing temperature. In order to achieve the complete order of magnetic moment, temperature must be decreased more lowly. Therefore, the Néel temperature decreases with increasing Al content in the tested alloys.

The variation of the observed SFE with Al content originates from the increases in the localized magnetic moment on the Fe atom sites and the anomaly in shear modulus caused by the addition of Al atoms. With increasing Al content, the average magnetic moment per atom increases, the anomaly in shear modulus appears, and the "ΔE" effect reduces in the tested alloys, therefore, the observed SFE increases slowly at 300 K. Once the Al content in austenitic Fe–Mn–Al alloy makes its Néel temperature decrease so lower that it is in the paramagnetic state at 300 K, then the observed SFE will be close to the non-magnetic component, such as alloy FA5.

As mentioned above, the decrease in the Néel temperature causes $-f^{\gamma}(\tau^{\gamma})$ to reduce with increasing Al content at 300 K, and the average magnetic moment per atom always increases. Since the magnetic component of SFE depends on the product of $\ln(\beta^{\gamma}+1)$ and $-f^{\gamma}(\tau^{\gamma})$, it shows a minimum value at a certain Al content, however, the magnetic component will continuously increases once Al content is more than this value.

Conclusions

1. The results obtained by the XRD profile analysis show that the SF probability decreases with increasing Al content, and the observed SFE increases linearly in the range of Al content lower than 6.27 at%, and markedly as it is more than 6.27 at%.
2. The thermodynamic estimation indicates that with increasing Al content the non-magnetic component of SFE increases faster than the observed SFE in the antiferromagnetic state, and the magnetic component depends on the average magnetic moment and Néel temperature at 300 K.
3. The inconsistency for the variations of the observed SFE and non-magnetic component with Al content results from the anomaly in shear modulus caused by the antiferromagnetic transition, and this anomaly is not considered in the thermodynamic estimation.
4. The increases in the localized magnetic moment on the Fe atom sites and the decrease in the Néel temperature are caused by the addition of Al and are accompanied by the anomaly in shear modulus, which is the reason for the effect of Al content on the SFE in the Fe–25Mn–(1.19–9.77)Al–0.68C (at%) alloys.

Acknowledgement The authors thank Professor Shuzhi LIN for his valuable help in the XRD testing and for the profitable discussion.

References

1. Ye CS (1977) Acta Metall Sin 13:149 (in Chinese)
2. Shih CH, Zhang YS et al (1984) Adv Cryog Eng Mater 31:161
3. Zhang YS, Su LJ (1983) Acta Metall Sin 19:A253 (in Chinese)
4. Zhang YS (1983) Acta Metall Sin 19:A262 (in Chinese)
5. Brüx U, Frommeyer G, Gràssel O, Meyer LW, Weise A (2002) Steel Res 73:294
6. Frommeyer G, Brüx U (2006) Steel Res 77:627
7. Tian X, Zhang YS, Shih CH (1986) Acta Metall Sin 22:A101 (in Chinese)
8. Sato K, Ichinase M, Hirotsu Y, Inoue Y (1989) ISIJ Inter 29:868. doi:10.2355/isijinternational.29.868
9. Takaki S, Furuya T, Tokunaga Y (1990) ISIJ Inter 30:632. doi:10.2355/isijinternational.30.632
10. Tian X, Zhang YS (1993) Scr Metall Mater 28:1219. doi:10.1016/0956-716X(93)90457-4
11. Zhu XM, Zhang YS (1998) Corrosion 54:3
12. Zhang YS, Lu X, Tian X, Qin ZX (2002) Mater Sci Eng A 334:19. doi:10.1016/S0921-5093(01)01781-6
13. Tian X, Tian R, Wei X, Zhang Y (2004) Can Metall Q 43:183
14. Zhang YS (1985) Acta Metall Sin 21:A295 (in Chinese)
15. Zhang YS (1986) Acta Metall Sin 22:A470 (in Chinese)
16. Sato A, Yamaji Y, Mori T (1986) Acta Metall 34:287. doi:10.1016/0001-6160(86)90199-9
17. Yang JH, Chen H, Wayman CM (1992) Metall Trans 23A:1445
18. Yang WS, Wan CM (1990) J Mater Sci 25:1821. doi:10.1007/BF01045392
19. Oh BW, Cho SJ, Kim YG et al (1995) Mater Sci Eng A 197:147. doi:10.1016/0921-5093(94)09751-8
20. Ruff AW Jr (1970) Metall Trans 1:2391
21. Gallagher PCJ (1970) Metall Trans 1:2429
22. Adler RPI, Otte HM, Wagner CNJ (1970) Metall Trans 1:2375
23. Reed RP, Schramm RE (1974) J Appl Phys 45:4705. doi:10.1063/1.1663122
24. Schramm RE, Reed RP (1975) Metall Trans 6A:1345
25. Mukherjee P, Sarkar A, Barat P et al (2004) Acta Mater 52:5687. doi:10.1016/j.actamat.2004.08.030
26. Kapoor K, Lahiri D et al (2005) Mater Charact 54:131. doi:10.1016/j.matchar.2004.09.009
27. Dey SN, Chatterjee P, Sen Gupta SP (2005) Acta Mater 53:4635. doi:10.1016/j.actamat.2005.06.017
28. Warren RE (1969) X-ray diffraction. Addison-Wesley, Reading, MA, p 251

29. Hirth JP (1970) Metall Trans 1:2367. doi:10.1007/BF02642816
30. Miodowink AP (1978) Calphad 2:207. doi:10.1016/0364-5916(78)90010-X
31. Ferreira PJ, Müllner P (1998) Acta Mater 46:4479. doi:10.1016/S1359-6454(98)00155-4
32. Lee YK, Choi CS (2000) Metall Mater Trans 31A:355. doi:10.1007/s11661-000-0271-3
33. Olson GB, Cohen M (1976) Metall Trans 7A:1897
34. Ishida K (1976) Phys Stat Solids 36:717. doi:10.1002/pssa.2210360233
35. Hirllert M, Jar M (1978) Calphad 2:227. doi:10.1016/0364-5916(78)90011-1
36. Tian X, Zhang YS (1991) Mater Sci Prog 5:48 (in Chinese)
37. Stepakoff GL, Kaufman L (1968) Acta Metall 16:13. doi:10.1016/0001-6160(68)90066-7
38. Breedis JF, Kaufman L (1971) Metall Trans 2:2359. doi:10.1007/BF02814874
39. Kaufman L, Nesor H (1978) Calphad 2:295. doi:10.1016/0364-5916(78)90018-4
40. Murr LE (1975) Interfacial phenomenon in metal and alloys. Addison-Wesley, Reading, MA, p 130
41. Ericsson T (1969) Acta Metall 14:1073. doi:10.1016/0001-6160(66)90195-7
42. Ishida K, Nishizawa T (1974) Trans Jpn Inst Met 15:225
43. Fernández Guillerment A (1987) High Temp High Press 19:477
44. Petrov Yu N, Yakubtsov IA (1986) Phys Met Metall 62(2):34
45. Ohno H, Mekata M (1971) J Phys Soc Jpn 31:102. doi:10.1143/JPSJ.31.102
46. Zhang YS (1988) J Phys Met Phys 18:L229
47. Qin ZX, Zhang YS (1998) Hyperfine Interact 116:225. doi:10.1023/A:1012670705310
48. Remy L, Pineau A (1977) Mater Sci Eng 28:99. doi:10.1016/0025-5416(77)90093-3
49. Umebayashi H, Ishikawa Y (1966) J Phys Soc Jpn 21:1281. doi:10.1143/JPSJ.21.1281